

## Durham Research Online

---

### Deposited in DRO:

06 August 2019

### Version of attached file:

Accepted Version

### Peer-review status of attached file:

Peer-reviewed

### Citation for published item:

Wang, Chao and Song, Shuguang and Wei, Chunjing and Su, Li and Allen, Mark B. and Niu, Yaoling and Li, Xian-Hua and Dong, Jinlong (2019) 'Palaeoarchaean deep mantle heterogeneity recorded by enriched plume remnants.', *Nature geoscience*, 12 (8). pp. 672-678.

### Further information on publisher's website:

<https://doi.org/10.1038/s41561-019-0410-y>

### Publisher's copyright statement:

---

### Use policy

The full-text may be used and/or reproduced, and given to third parties in any format or medium, without prior permission or charge, for personal research or study, educational, or not-for-profit purposes provided that:

- a full bibliographic reference is made to the original source
- a [link](#) is made to the metadata record in DRO
- the full-text is not changed in any way

The full-text must not be sold in any format or medium without the formal permission of the copyright holders.

Please consult the [full DRO policy](#) for further details.

**Palaeoarchaeoan Deep Mantle Heterogeneity Recorded by  
3.45 Ga Enriched Plume Remnants**

Chao Wang<sup>1,2\*</sup>, Shuguang Song<sup>1\*</sup>, Chunjing Wei<sup>1</sup>, Li Su<sup>3</sup>, Mark B. Allen<sup>4</sup>, Yaoling  
Niu<sup>2,4</sup>, Xian-Hua Li<sup>5</sup>, Jinlong Dong<sup>1</sup>

<sup>1</sup> *MOE Key Laboratory of Orogenic Belts and Crustal Evolution, School of Earth and  
Space Sciences, Peking University, Beijing 100871, China*

<sup>2</sup> *School of Earth Sciences and Resources, China University of Geosciences, Beijing  
100083, China*

<sup>3</sup> *School of Scientific Research and State Key Laboratory of Geological Processes and  
Mineral Resources, China University of Geosciences, Beijing 100083, China*

<sup>4</sup> *Department of Earth Sciences, Durham University, Durham DH1 3LE, UK*

<sup>5</sup> *State Key Laboratory of Lithospheric Evolution, Institute of Geology and  
Geophysics, Chinese Academy of Sciences, Beijing 100029, China*

Revised manuscript for *Nature Geoscience*

\*corresponding authors

Chao Wang (chao.wang@cugb.edu.cn)

Shuguang Song (sgsong@pku.edu.cn)

21 **Cover note**

22 **Length of title:** 84 characters including spaces.

23 **Length of abstract:** 175 words.

24 **Length of main text:** 2598 words.

25 **Length of sub-headings:** sub-heading #1, 34 characters including spaces; sub-heading

26 #2, 42 characters including spaces; sub-heading #3, 57 characters including spaces.

27 **Length of methods:** 1491 words.

28 **Length of legends:** Figure 1, 79 words; Figure 2, 106 words; Figure 3, 120 words;

29 Figure 4, 52 words; Figure 5, 134 words.

30 **Number of references for main text (including legends):** 42 references.

31 **Number of references for methods:** 18 references.

32 **Number of references for Supplementary Information:** 8 references.

33 **Number and estimated final size of figures and tables:** 5 Figures; Figures 1–3 need

34 to be of two-column width; Figures 4–5 need to be of one-column width. 10

35 Supplementary Figures and 6 Supplementary Tables; all of them will be deposited in

36 Supplementary Information files.

37

## 38    **Abstract**

39    The thermal and chemical state of the early Archaean deep mantle is poorly resolved  
40    due to rare occurrences of early Archaean highly magnesian volcanic rocks. Here we  
41    report the first discovery of a suite of Palaeoarchaeon (3.45 Ga in situ zircon U-Pb age)  
42    ultramafic-mafic rocks with mantle plume signatures in Longwan, Eastern Hebei, the  
43    North China Craton. This suite consists of high-grade metamorphic lherzolite,  
44    pyroxenite, ferropicrite and ferrobasalt. The meta-ferropicrite and meta-ferrobasalt  
45    show geochemical characteristics of present-day oceanic island basalt and unusually  
46    high mantle potential temperatures ( $T_p = 1,675\text{ }^{\circ}\text{C}$ ), suggesting a deep mantle source  
47    enriched in iron and incompatible elements. The Longwan ultramafic-mafic suite is  
48    best interpreted as representing remnants of 3.45 Ga mantle plume magmatism. The  
49    first emergence of mantle plume-related rocks with various deep mantle sources on  
50    the Earth took place at 3.5–3.45 Ga, implying that a global mantle plume event  
51    occurred with the onset of large-scale deep mantle convection in the Palaeoarchaeon,  
52    and significant compositional heterogeneity, most likely introduced by recycled  
53    crustal material, was present in the Palaeoarchaeon deep mantle.

54

55 Highly magnesian lavas (e.g., komatiites and picrites) are rare in Earth history, and  
56 are typically produced by adiabatic decompression melting of upwelling mantle  
57 plumes that are significantly hotter than the ambient mantle<sup>1-3</sup>. Because of the close  
58 affinity of komatiites and picrites with their primary magmas, they can probe the  
59 thermal and chemical state of the Earth's thermal boundary layer from which mantle  
60 plumes originate through time<sup>4-6</sup>. Ultramafic rocks occur in the 3.8 Ga greenstone  
61 belts of the North Atlantic Craton, but accumulated evidence indicates that these  
62 rocks were not mantle plume-related<sup>7-10</sup>. Definite records of mantle plume activities  
63 began to emerge since ~3.5 Ga<sup>1,2</sup>, including 3.5–3.46 Ga komatiites in the  
64 Onverwacht Group, Barberton, South Africa and Coonterunah, East Pilbara, Australia.  
65 Geochemistry of Archaean komatiites suggests that their deep mantle source was hot,  
66 and depleted or similar to primitive mantle, while geochemistry of post-Archaean  
67 komatiites indicates a colder and heterogeneous deep mantle reservoir with enriched  
68 components introduced by Earth's convection<sup>4,5</sup>. There are no records of enriched  
69 ultramafic rocks from the Palaeoarchaeon (3.6–3.2 Ga), comparable to the picrites  
70 associated with Phanerozoic mantle plumes, but given the fragmentary nature of the  
71 geological record, it is not clear whether this reflects a genuine lack of deep mantle  
72 heterogeneity and deep mantle convection in the Palaeoarchaeon, or a sampling bias.

73 Here we report for the first time a suite of Palaeoarchaeon ultramafic-mafic rocks  
74 with a lithological assemblage of metamorphosed lherzolite, pyroxenite, ferropicrite  
75 and ferrobasalt in the North China Craton (NCC). Geochronological and geochemical  
76 evidence indicates that these ultramafic-mafic rocks are remnants of a 3.45 Ga

77 enriched mantle plume. Based on these findings, we propose that a global mantle  
78 plume event occurred in the Palaeoarchaeon as a result of large-scale deep mantle  
79 convection, and significant compositional heterogeneity was present in the  
80 Palaeoarchaeon deep mantle.

## 81 **The Longwan ultramafic-mafic suite**

82 The NCC is a rare craton in that it preserves  $\geq 3.8$  Ga crustal record, both from extant  
83 orthogneisses and from detrital zircons in younger metasedimentary rocks<sup>11</sup>. There  
84 was widespread Neoarchaeon granulite-facies metamorphism and granitic magmatism  
85 as the result of micro-continental collision<sup>12–14</sup>. No Eoarchaeon–Palaeoarchaeon  
86 mantle-derived ultramafic-mafic rocks, especially mantle plume-related  
87 ultramafic-mafic rocks, have been reported before from the NCC. The studied  
88 ultramafic-mafic rocks were collected from the Longwan iron-mining area of Eastern  
89 Hebei in the Eastern Block of the NCC (Fig. 1a). The Longwan ultramafic-mafic suite,  
90 together with banded (or massive) iron quartzite and garnet-mica schist, occurs as  
91 hundreds-metre to kilometre-scaled tectonic slivers within Neoarchaeon  
92 tonalite-trondhjemite-granodiorite (TTG) gneisses (Fig. 1b). The iron quartzite lenses  
93 have been mined, and the ultramafic-mafic rocks crop out as dark-coloured wall-rocks  
94 of the mining pits. Two major types of ultramafic-mafic rocks have been identified  
95 based on their mineral assemblages: (1) meta-cumulates and (2) meta-basalts. They  
96 were all metamorphosed and completely recrystallized under high-pressure (HP)  
97 granulite-facies metamorphism at the end of the Neoarchaeon, and no primary igneous

198 textures remain. The meta-cumulates occur as lens-shaped blocks and are  
199 meta-lherzolite and meta-websterite in composition (Supplementary Fig. 1a–c), and  
100 strongly recrystallized samples developed an idioblastic texture with triple junction  
101 grain boundaries close to 120° angles (Supplementary Fig. 2a–b). The meta-lherzolite  
102 is a rare component in the meta-cumulates and has a mineral assemblage of olivine,  
103 clinopyroxene, orthopyroxene, minor Al-rich spinel and opaque oxides  
104 (Supplementary Fig. 2a). The meta-websterite consists of clinopyroxene,  
105 orthopyroxene, amphibole, with accessory pyrite between them (Supplementary Fig.  
106 2b). The meta-basalts are dark- to green-coloured massive outcrops (Supplementary  
107 Fig. 1d–e) and mafic in composition. They were metamorphosed into two-pyroxene  
108 granulites (clinopyroxene, orthopyroxene, plagioclase, quartz and opaque oxides) or  
109 garnet-clinopyroxene granulites (garnet, clinopyroxene, plagioclase, quartz and  
110 opaque oxides) (Supplementary Fig. 2c–d) with very weak or no foliation. All zircon  
111 grains from meta-basalts are metamorphic without any magmatic cores, giving  
112 metamorphic ages of ~2.5 Ga as a result of intensive Neoarchaeon granulite-facies  
113 tectonothermal events (our unpublished data).

114       One hundred and twenty-five zircon grains were extracted from a meta-websterite  
115 sample J14-46c (~30 kg) of the Longwan ultramafic-mafic suite. Zircons are mostly  
116 subhedral crystals, 50–100 µm in length and show clear core-rim textures; bright  
117 cores with weakly oscillatory zoning are surrounded by dark rims in  
118 cathodoluminescence (CL) images (Fig. 2a), indicative of metamorphic overgrowth  
119 around magmatic cores<sup>15</sup>. There are apatite inclusions in the magmatic cores, but no

felsic mineral inclusions were identified within them (Supplementary Fig. 3).  
 Twenty-eight magmatic cores and 17 metamorphic rims were analyzed, and U-Pb  
 data are listed in Supplementary Table 1. Most analyses are discordant owing to lead  
 loss and plot under the concordia curve (Fig. 2b). Twenty-eight magmatic cores yield  
 a  $^{207}\text{Pb}/^{206}\text{Pb}$  age range of  $3,475 \pm 14$  to  $3,302 \pm 2$  Ma ( $1\sigma$ ) with Th/U ratios generally  
 over 0.2. They lie along a discordant line that intersects the concordia at  $3,456 \pm 15$   
 Ma with a mean square weighted deviation (MSWD) of 1.9 (Fig. 2b), which is in  
 accordance with the concordia age ( $3,451 \pm 3$  Ma; MSWD = 0.36) and weighted mean  
 $^{207}\text{Pb}/^{206}\text{Pb}$  age ( $3,454 \pm 4$  Ma; MSWD = 8.1) of 13 analyses indistinguishable from  
 the concordia curve (Fig. 2c). Most of the concordant analyses have Th/U ratios  
 above 1. Seventeen metamorphic rims give  $^{207}\text{Pb}/^{206}\text{Pb}$  ages ranging between  $3,279 \pm$   
 $4$  to  $2,993 \pm 22$  Ma with Th/U ratios mostly below 0.1. They define a discordant line  
 intercepting the concordia at  $3,267 \pm 20$  Ma (MSWD = 3.9), with three concordant  
 $^{207}\text{Pb}/^{206}\text{Pb}$  ages of  $3,271 \pm 1$  to  $3,238 \pm 2$  Ma. Nine concordant magmatic cores were  
 chosen for in situ trace element analyses, and the data are listed in Supplementary  
 Table 2. Their trace element ratios are typical of zircons from mantle-derived magma,  
 and resemble zircons from plume-influenced settings (Supplementary Fig. 4).  
 Thirteen concordant to near-concordant magmatic cores (discordance < 10%) from  
 the meta-websterite sample J14-46c were selected for in situ Hf-O isotope analyses,  
 and data are listed in Supplementary Table 3. These magmatic cores have initial  
 $^{176}\text{Hf}/^{177}\text{Hf}$  ratios of 0.280569–0.280720 (calculated at the concordia age  $3451 \pm 3$  Ma)  
 with  $\epsilon_{\text{Hf}}(t)$  values of 0.2 to 5.6, and have mantle-like  $\delta^{18}\text{O}$  values from 4.10‰ to 5.58‰



142 (Fig. 2d).

143 Bulk-rock major and trace element data of the studied samples are listed in  
144 Supplementary Table 4. Samples of the Longwan ultramafic-mafic suite have  
145 systematic compositional variation as shown in MgO-variation diagrams  
146 (Supplementary Fig. 5). The meta-lherzolite samples have low contents of SiO<sub>2</sub>  
147 (39.84–44.86 wt.%) and Al<sub>2</sub>O<sub>3</sub> (3.80–5.44 wt.%), but high MgO (27.76–33.03 wt.%)  
148 and Mg# (84.1–85.3) (Fig. 3b). They are slightly enriched in light rare earth elements  
149 (LREEs) over heavy rare earth elements (HREEs) with (La/Yb)<sub>N</sub> ranging from 2.7 to  
150 4.7 (Fig. 3d). These meta-lherzolites have high abundances of compatible elements  
151 such as Cr and Ni. The meta-websterites are characterized by high contents of SiO<sub>2</sub>  
152 (51.15–54.18 wt.%), MgO (23.28–26.55 wt.%) with accordingly high Mg# (85.5–86.8)  
153 (Fig. 3b), and compatible elements (e.g., Cr and Ni). They are relatively low in TiO<sub>2</sub>  
154 (0.13–0.16 wt.%), Al<sub>2</sub>O<sub>3</sub> (3.56–4.08 wt.%) and Fe<sub>2</sub>O<sub>3T</sub> (8.30–8.91 wt.%). They have  
155 similar trace element patterns compared with the meta-lherzolite samples (Fig. 3d).  
156 They show relative depletion of high field strength elements (HFSEs; e.g., Nb, Ta, Zr  
157 and Hf) (Fig. 3d). All the meta-basalts are iron-rich with Fe<sub>2</sub>O<sub>3T</sub> mostly > 14 wt.%  
158 and variable MgO contents (7.29–19.36 wt.%), and plot in the ‘Alkali basalt’ field  
159 (Fig. 3a). According to their MgO contents, they can be further subdivided into  
160 meta-ferropicrites (MgO > 12 wt.%) and meta-ferrobasalts (MgO < 12 wt.%). The  
161 meta-ferropicrites have high contents of TiO<sub>2</sub> (1.61–2.10 wt.%), MgO (12.57–19.36  
162 wt.%), Cr (1,162–1,494 ppm) and Ni (411–943 ppm) with SiO<sub>2</sub> of 43.73–49.78 wt.%  
163 and Mg# of 62.1–71.9 (Fig. 3b). They are relatively enriched in Fe<sub>2</sub>O<sub>3T</sub> (15.24–16.89

164 wt.%) (Fig. 3c) but low in  $\text{Al}_2\text{O}_3$  (4.65–7.85 wt.%). Their REE abundances are much  
165 higher than those of meta-cumulates, and they also show enrichment of LREEs over  
166 HREEs ( $(\text{La/Yb})_{\text{N}} = 6.7\text{--}8.6$ ), ranging between the enriched mid-ocean ridge basalt  
167 (E-MORB) and the ocean island basalt (OIB) but having a closer affinity with OIB.  
168 They are depleted in Y and some HFSEs (e.g., Zr and Hf), but have positive  
169 anomalies of Nb and Ta (Fig. 3d). The meta-ferrobasalts have similar geochemical  
170 features to the meta-ferropicrites, except that they have lower MgO (7.29–9.36 wt.%)  
171 and  $\text{Fe}_2\text{O}_{3\text{T}}$  (11.19–15.68 wt.%) with Mg# of 50.6–62.0 and relatively high  $\text{Al}_2\text{O}_3$   
172 (6.80–11.05 wt.%) and CaO (14.36–18.05 wt.%). They also have relatively high  
173 abundances of Cr (825–1,394 ppm) and Ni (499–839 ppm).

## 174 **Remnants of Palaeoarchaeon plume magmatism**

175 The absence of felsic mineral inclusions (Supplementary Fig. 3), and the sharp  
176 contrast of age population, Th/U ratios and  $\varepsilon_{\text{Hf}}(t)$  values between magmatic zircon  
177 cores from the meta-websterite sample J14-46c and pre-2.8 Ga detrital or xenocrystic  
178 zircons from Eastern Hebei (Supplementary Figs. 6 and 7) argue against a xenocrystic  
179 origin of these zircons. Instead, morphological characteristics in CL images, high  
180 Th/U ratios, trace element systematics with close plume affinity and mantle-like Hf-O  
181 isotopic compositions demonstrate that these zircon cores were crystallized from  
182 mantle-derived magma at ~3.45 Ga (Fig. 2 and Supplementary Fig. 4). Even though  
183 the Longwan ultramafic-mafic rocks experienced HP granulite-facies metamorphism  
184 at the end of the Neoarchaeon, most of their trace elements (e.g., REEs and HFSEs)

185 were relatively immobile during the Neoarchaean orogenic events, because these  
186 elements have positive linear correlations with Zr (Supplementary Fig. 8). The high  
187 Cr and Ni concentrations of meta-basalts argue that their elevated MgO contents are  
188 of original magmatic significance without metamorphic modification.

189 The meta-websterites are unlike any ultramafic-mafic lavas (e.g., komatiites,  
190 picrites and boninites), but similar to experimental and natural pyroxenite  
191 cumulates<sup>16,17</sup> (Fig. 3b), suggesting that they were crystallized from MgO-rich melts.  
192 The meta-lherzolites are also of cumulate origin, evidenced by their identical trace  
193 element patterns to meta-websterites (Fig. 3d). The correlation of Ni and V against Cr  
194 of the meta-basalts (Supplementary Fig. 9) implies that their protolith magmas  
195 experienced clinopyroxene-dominated (with olivine) fractionation. In addition, the  
196 meta-cumulates and the meta-basalts show complementary trends on Harker diagrams  
197 (Supplementary Fig. 5) and have almost indistinguishable ratios of Nb/Ta, Zr/Hf and  
198 Tb/Dy (Supplementary Fig. 10). Thus, it is highly likely that meta-cumulates were  
199 crystallized from the same magmas parental to the meta-basalts when ascending and  
200 cooling to shallower magma chambers. Using bulk-rock Mg# of the meta-cumulates  
201 and Fe-Mg exchange coefficients, we calculate Mg# and liquidus temperatures of the  
202 melts crystallizing cumulus minerals (see Methods). The results show that protoliths  
203 of the meta-cumulates were crystallized from relatively evolved melts with Mg# of  
204 62.2–67.8 at temperature of ca. 1200 °C (Supplementary Table 5). As for their  
205 crystallizing pressures, the lack of garnet in the meta-cumulates and their low Al<sub>2</sub>O<sub>3</sub>  
206 contents point to a shallow depth at least below the garnet stability field, i.e.,

207 spinel/plagioclase stability fields (~1–2 GPa).

208       The elevated iron contents of the meta-ferropicrites are distinguishable from  
209 typical picrites/komatiites but similar to iron-rich ferropicrites/ferrokomatiites (Fig.  
210 3c). The meta-ferrobasalts (MgO < 12 wt.%) have similar elevated iron contents and  
211 trace element characteristics with the meta-ferropicrites (Fig. 3). The meta-basalts are  
212 all enriched in compatible elements (Cr, Co and Ni), suggesting a derivation from  
213 relatively high-degree melting of the mantle source. They are also enriched in Nb, Ta,  
214 Ti and LREEs, and their trace element patterns are similar to those of present-day OIB,  
215 indicative of an enriched mantle source (Fig. 3d). The uniformly high (Gd/Yb)<sub>N</sub>, low  
216 Al<sub>2</sub>O<sub>3</sub>/TiO<sub>2</sub> ratios and Zr-Hf depletion indicate the presence of residual garnet in their  
217 mantle source as garnet prefers to hold Zr, Hf, HREEs and Al<sub>2</sub>O<sub>3</sub> at high pressures  
218 (Figs. 3d and 4a). Their MgO-CaO systematics show that they were primarily derived  
219 from peridotite source with minor contribution from pyroxenite<sup>18</sup> (Fig. 4b). Therefore,  
220 the meta-ferropicrites have close affinity with primary magmas, while the  
221 meta-ferrobasalts with lower MgO and Mg# could represent evolved melts from those  
222 of the meta-ferropicrites after fraction of clinopyroxene and olivine (Supplementary  
223 Fig. 9).

224       Using FractionatePT software<sup>19</sup>, we calculate melting conditions for primary  
225 magmas of the most primitive meta-ferropicrite samples (Supplementary Table 6) and  
226 results indicate that their primary magmas were derived from melting of mantle  
227 lherzolite at high pressures/temperatures (P = 5.7–6.7 GPa, T = 1,756–1,776 °C) (Fig.  
228 5), corresponding to a mantle potential temperature (T<sub>p</sub>) of 1,725 °C. However,

229 experimental studies have demonstrated that iron-rich lherzolites have systematically  
230 lower solidus temperatures than fertile peridotites by  $\sim 50$  °C<sup>20</sup>, and thus the  $T_p$  for the  
231 meta-ferropicrites should be conservatively corrected to be 1,675 °C. The melting  
232 conditions and  $T_p$  are comparable to those for Palaeoarchaean komatiites in Barberton  
233 and East Pilbara (Fig. 5). The above lines of evidence clearly point to a derivation of  
234 primary magmas of the meta-basalts through melting of an anomalously hot mantle  
235 source at high pressures.

236 It is well accepted that the thermal regime in the Archaean was hotter than the  
237 present<sup>21</sup>. However, the estimated  $T_p$  for the Longwan meta-ferropicrites is 1,675 °C,  
238 implying that their mantle source was considerably hotter than the ambient mantle  
239 with  $T_p$  of 1,500–1,600 °C at 3.45 Ga<sup>5</sup>. Such conditions, when ascending mantle  
240 material is significantly hotter than the surrounding mantle, are consistent with the  
241 mantle plume model<sup>22,23</sup>. Besides, the high Ni contents of the Longwan meta-basalts  
242 argue for a strong affinity to mantle plume-related rocks than their lower-temperature  
243 counterparts<sup>4</sup>. Ferropicrites are rare throughout the geological history, and most  
244 Phanerozoic ferropicrite examples were identified at or near the base of volcanic  
245 sequences in continental large igneous province (LIP) or continental flood basalt  
246 province settings, with a few cases in accreted oceanic plateaus<sup>24,25</sup>. It is generally  
247 acknowledged that LIPs result from the arrival of a mantle plume head at the base of  
248 the lithosphere<sup>26–28</sup>. Thus, it is most likely that the Longwan ultramafic-mafic suite  
249 represents remnants of dismembered volcanic successions generated during a  
250 Palaeoarchaean ( $\sim 3.45$  Ga) mantle plume activity.

## 251 **Implications for Palaeoarchaean deep mantle** 252 **heterogeneity**

253 Mantle plume activities were infrequent through the Archaean compared with the  
254 Proterozoic and the Phanerozoic<sup>29</sup>. Komatiites and komatiitic basalts were generated  
255 by adiabatic decompression melting of upwelling mantle plumes at high mantle  
256 potential temperatures and pressures, and serve as records of mantle plume  
257 activities<sup>2,5</sup>. The 3.45 Ga Longwan ultramafic-mafic suite reported in this study, and  
258 the 3.5–3.46 Ga komatiites preserved in Barberton and East Pilbara, are the oldest  
259 confirmed records of mantle plume activities<sup>1,2</sup>. These Palaeoarchaean mantle  
260 plume-related rocks could be a record of the oldest global mantle plume event in the  
261 Earth's history and a counterpart to younger occurrences of global mantle plume  
262 activities<sup>30</sup>. This global mantle plume event may indicate that large-scale deep mantle  
263 convection has been operating since the Palaeoarchaean.

264 Partial melting of a typical peridotitic mantle alone cannot explain the iron-rich  
265 features observed in ferropicrites<sup>24,31–33</sup>. It is commonly suggested that Archaean  
266 ferropicrites required an iron-rich peridotitic mantle source, though how to reach this  
267 iron enrichment remains controversial: addition of recycled crustal material, an  
268 initially iron-rich mantle and subsequent iron sequestration, a core contribution and  
269 even an infall of iron-rich chondritic meteorites<sup>24,31–37</sup>. Nonetheless, the occurrence of  
270 meta-ferropicrites and meta-ferrobasalts in the ~3.45 Ga Longwan ultramafic-mafic  
271 suite indicates the existence of iron-rich domains in their Palaeoarchaean deep mantle  
272 source. In addition, the enriched REE patterns and the relatively high melting degrees

273 of these meta-ferropicrites and meta-ferrobasalts require an enriched deep mantle  
274 source, whereas the depleted and flat REE patterns of the 3.5–3.46 Ga komatiites in  
275 Barberton and East Pilbara imply a depleted or primitive deep mantle source<sup>1,2,4</sup> (Fig.  
276 3d). Therefore, deep mantle heterogeneity was present in the Palaeoarchaeon, with  
277 partial enrichment of iron and incompatible elements. Enriched domains in the  
278 Palaeoarchaeon deep mantle are most probably caused by the incorporation of  
279 recycled crustal material<sup>24,25,31</sup>, and indicate interaction between lithosphere and  
280 mantle plumes, and crustal recycling processes.

## 281 **Figure legends**

282 **Figure 1 Geological maps of Eastern Hebei, the NCC and the study area.** **a**, Inset  
283 is a sketch map of the NCC showing its major tectonic units. Eastern Hebei lies in the  
284 Eastern Block of the NCC and its Precambrian basement rocks consist of  
285 Neoarchaeon TTG gneisses, charnockites, and supracrustal rocks with some  
286 Palaeo-Mesoarchaeon supracrustal remnants and Palaeoproterozoic mafic dykes. **b**,  
287 The studied meta-cumulate and meta-basalt samples were collected from  
288 meta-supracrustal lenses from the Longwan iron-mining area of Eastern Hebei, which  
289 are within the Neoarchaeon TTG gneisses and intruded by Mesozoic plutons.

290

291 **Figure 2 CL images, U-Pb concordia diagrams and Hf-O isotopes for zircons**  
292 **from the meta-websterite sample J14-46c the Palaeoarchaeon Longwan**  
293 **ultramafic-mafic suite.** **a**, CL images of representative zircons from the

meta-websterite sample J14-46c; ellipses are in situ SIMS zircon U-Pb analytical spots; numbers in ellipses are sequential numbers of analytical spots; ages next to ellipses are zircon  $^{207}\text{Pb}/^{206}\text{Pb}$  ages; scale bars are 20  $\mu\text{m}$  in length. **b**, U-Pb concordia diagram for all zircons from the meta-websterite sample J14-46c. **c**, U-Pb concordia diagram for concordant magmatic zircon cores from the meta-websterite sample J14-46c; inset is the weighted mean  $^{207}\text{Pb}/^{206}\text{Pb}$  age of concordant magmatic zircon cores. **d**,  $\varepsilon_{\text{Hf}}(t)$ - $\delta^{18}\text{O}$  diagram for magmatic zircon cores with discordance < 10% from the meta-websterite sample J14-46c; mantle zircon  $\delta^{18}\text{O}$  values are from ref. 38.

**Figure 3 Geochemical diagrams for the Palaeoarchaeon Longwan ultramafic-mafic suite.** **a**, Rock classification diagram<sup>39</sup> for meta-basalts with meta-cumulates plotted for comparison. **b**,  $\text{SiO}_2$ -MgO diagram; fields of komatiites, picrites, basalts and bonnites are constructed using the data from the GEOROC database with experimentally-produced pyroxenite cumulates<sup>16</sup> plotted for comparison. **c**,  $\text{SiO}_2$ -FeOt diagram; fields of ferropicrite/ferrokomatiite, picrite/komatiite and Iceland/MORB are from ref. 24. Major element oxides in **a**, **b** and **c** are recalculated on an anhydrous basis. **d**, Primitive mantle-normalized trace element diagram; values of primitive mantle, OIB and E-MORB are from ref. 40 and values of 3.5–3.46 Ga komatiites in Barberton and East Pilbara are from ref. 3; only fluid immobile elements are plotted because they should not have been affected during high-grade metamorphism and can be used for petrogenetic interpretations.



316 **Figure 4 Geochemical diagrams for the meta-basalts of the Palaeoarchaean**  
317 **Longwan ultramafic-mafic suite. a,**  $\text{Al}_2\text{O}_3/\text{TiO}_2-(\text{Gd}/\text{Yb})_{\text{N}}$  diagram after ref. 41; N  
318 denotes chondrite-normalized; chondrite and OIB values are from ref. 40. **b,**  
319 **MgO-CaO diagram after ref. 18; the dashed line is the boundary to differentiate**  
320 **between peridotite-sourced melts (above the line) and pyroxenite-sourced melts**  
321 **(below the line). Major element oxides are recalculated on an anhydrous basis.**

322

323 **Figure 5 Calculated melting conditions for primary magmas of the**  
324 **meta-ferropicrites of the Palaeoarchaean Longwan ultramafic-mafic suite.**  
325 Melting conditions for primary magmas of the most primitive meta-ferropicrite  
326 samples with the highest MgO contents (15LW-13 and 17LW-08) are calculated using  
327 thermobarometers based on magma Si and Mg contents<sup>19</sup>. Potential temperatures ( $T_p$ )  
328 are estimated by back-calculating melting conditions of primary magmas along an  
329 isentropic melting adiabat until the melting adiabat intersects the solidus and then  
330 extrapolating from this intersection point along a solid mantle adiabat to the surface.  
331 Dry lherzolite solidus and liquidus are from ref. 42; Fe-rich lherzolite solidus (heavy  
332 dashed line) is estimated via lowering the dry lherzolite solidus by  $\sim 50^\circ\text{C}$ <sup>20</sup>; blue  
333 near-vertical lines represent solid mantle adiabats with varying mantle potential  
334 temperatures ( $T_p$ ); the red curved line with arrow corresponds to the isentropic  
335 melting adiabat; melting conditions for MORB, Hawaii Hotspot basalt and  
336 Palaeoarchaean komatiite are from ref. 19.

## 337 Online content

338 Methods, including statements of data availability and associated references, and  
339 Supplementary Information files are available in the online version of this paper.

## 340 References

- 341 1. Arndt NT, Leshar CM, Barnes SJ. *Komatiite*. Cambridge University Press, 2008.
- 342 2. Barnes SJ, Arndt NT. Chapter 6 - Distribution and geochemistry of komatiites and  
343 basalts through the Archean. In: Van Kranendonk MJ, Bennett VC, Hoffmann JE  
344 (eds). *Earth's Oldest Rocks (Second Edition)*. Elsevier, 2019, pp 103-132.
- 345 3. Sossi PA, Eggins SM, Nesbitt RW, Nebel O, Hergt JM, Campbell IH, *et al.*  
346 Petrogenesis and Geochemistry of Archean Komatiites. *Journal of Petrology* 2016,  
347 **57**(1): 147-184.
- 348 4. Campbell I, Griffiths R. The changing nature of mantle hotspots through time:  
349 implications for the chemical evolution of the mantle. *The Journal of Geology*  
350 1992, **100**(5): 497-523.
- 351 5. Herzberg C, Condie K, Korenaga J. Thermal history of the Earth and its  
352 petrological expression. *Earth and Planetary Science Letters* 2010, **292**(1-2):  
353 79-88.
- 354 6. Nisbet EG, Cheadle MJ, Arndt NT, Bickle MJ. Constraining the potential  
355 temperature of the Archaean mantle: A review of the evidence from komatiites.  
356 *Lithos* 1993, **30**(3): 291-307.
- 357 7. Dymek RF, Brothers SC, Schiffries CM. Petrogenesis of Ultramafic Metamorphic

- 358 Rocks from the 3800 Ma Isua Supracrustal Belt, West Greenland. *Journal of*  
359 *Petrology* 1988, **29**(6): 1353-1397.
- 360 8. Collerson KD, Campbell LM, Weaver BL, Palacz ZA. Evidence for extreme mantle  
361 fractionation in early Archaean ultramafic rocks from northern Labrador. *Nature*  
362 1991, **349**: 209-214.
- 363 9. Polat A, Hofmann AW, Rosing MT. Boninite-like volcanic rocks in the 3.7–3.8 Ga  
364 Isua greenstone belt, West Greenland: geochemical evidence for intra-oceanic  
365 subduction zone processes in the early Earth. *Chemical Geology* 2002, **184**(3–4):  
366 231-254.
- 367 10. O’Neil J, Francis D, Carlson RW. Implications of the Nuvvuagittuq Greenstone  
368 Belt for the Formation of Earth’s Early Crust. *Journal of Petrology* 2011, **52**(5):  
369 985-1009.
- 370 11. Liu DY, Nutman AP, Compston W, Wu JS, Shen QH. Remnants of  $\geq 3800$  Ma  
371 crust in the Chinese part of the Sino-Korean craton. *Geology* 1992, **20**(4):  
372 339-342.
- 373 12. Nutman AP, Wan Y, Du L, Friend CRL, Dong C, Xie H, *et al.* Multistage late  
374 Neoarchaean crustal evolution of the North China Craton, eastern Hebei.  
375 *Precambrian Research* 2011, **189**(1–2): 43-65.
- 376 13. Zhai M-G, Santosh M, Zhang L. Precambrian geology and tectonic evolution of  
377 the North China Craton. *Gondwana Research* 2011, **20**(1): 1-5.
- 378 14. Wang C, Song S, Niu Y, Wei C, Su L. TTG and Potassic Granitoids in the Eastern  
379 North China Craton: Making Neoproterozoic Upper Continental Crust during

- 380       Micro-continental Collision and Post-collisional Extension. *Journal of Petrology*  
381       2016, **57**(9): 1775-1810.
- 382   15. Corfu F, Hanchar JM, Hoskin PW, Kinny P. Atlas of zircon textures. *Reviews in*  
383       *Mineralogy and Geochemistry* 2003, **53**(1): 469-500.
- 384   16. Müntener O, Kelemen PB, Grove TL. The role of H<sub>2</sub>O during crystallization of  
385       primitive arc magmas under uppermost mantle conditions and genesis of igneous  
386       pyroxenites: an experimental study. *Contributions to Mineralogy and Petrology*  
387       2001, **141**(6): 643-658.
- 388   17. Lee C-TA, Cheng X, Horodyskyj U. The development and refinement of  
389       continental arcs by primary basaltic magmatism, garnet pyroxenite accumulation,  
390       basaltic recharge and delamination: insights from the Sierra Nevada, California.  
391       *Contributions to Mineralogy and Petrology* 2006, **151**(2): 222-242.
- 392   18. Herzberg C, Asimow PD. Petrology of some oceanic island basalts:  
393       PRIMELT2.XLS software for primary magma calculation. *Geochemistry,*  
394       *Geophysics, Geosystems* 2008, **9**(9): Q09001.
- 395   19. Lee C-TA, Luffi P, Plank T, Dalton H, Leeman WP. Constraints on the depths and  
396       temperatures of basaltic magma generation on Earth and other terrestrial planets  
397       using new thermobarometers for mafic magmas. *Earth and Planetary Science*  
398       *Letters* 2009, **279**(1-2): 20-33.
- 399   20. Kushiro I. Partial Melting of a Fertile Mantle Peridotite at High Pressures: An  
400       Experimental Study Using Aggregates of Diamond. *Earth Processes: Reading*  
401       *the Isotopic Code*, vol. 95, 1996, pp 109-122.

- 402 21. Richter FM. Models for the Archean thermal regime. *Earth and Planetary Science*  
403 *Letters* 1985, **73**(2-4): 350-360.
- 404 22. Campbell IH, Griffiths RW, Hill RI. Melting in an Archaean mantle plume: heads  
405 it's basalts, tails it's komatiites. *Nature* 1989, **339**: 697-699.
- 406 23. Campbell IH, Griffiths RW. Implications of mantle plume structure for the  
407 evolution of flood basalts. *Earth and Planetary Science Letters* 1990, **99**(1):  
408 79-93.
- 409 24. Gibson SA. Major element heterogeneity in Archean to Recent mantle plume  
410 starting-heads. *Earth and Planetary Science Letters* 2002, **195**(1): 59-74.
- 411 25. Jennings ES, Holland TJB, Shorttle O, MacLennan J, Gibson SA. The  
412 Composition of Melts from a Heterogeneous Mantle and the Origin of Ferropicrite:  
413 Application of a Thermodynamic Model. *Journal of Petrology* 2016, **57**(11-12):  
414 2289-2310.
- 415 26. Coffin MF, Eldholm O. Large igneous provinces: Crustal structure, dimensions,  
416 and external consequences. *Reviews of Geophysics* 1994, **32**(1): 1-36.
- 417 27. Saunders AD. Large igneous provinces: origin and environmental consequences.  
418 *Elements* 2005, **1**(5): 259-263.
- 419 28. Ernst RE, Jowitt SM. Large igneous provinces (LIPs) and metallogeny. *Tectonics,*  
420 *Metallogeny, and Discovery: the North American Cordillera and Similar*  
421 *Accretionary Settings Edited by M Colpron, T Bissig, BG Rusk, and JFH*  
422 *Thompson Society of Economic Geologists Special Publication* 2013, **17**: 17-51.
- 423 29. Ernst R, Bleeker W. Large igneous provinces (LIPs), giant dyke swarms, and

- mantle plumes: significance for breakup events within Canada and adjacent regions from 2.5 Ga to the Present. *Canadian Journal of Earth Sciences* 2010, **47**(5): 695-739.
30. Barley ME, Krapez B, Groves DI, Kerrich R. The Late Archaean bonanza: metallogenic and environmental consequences of the interaction between mantle plumes, lithospheric tectonics and global cyclicity. *Precambrian Research* 1998, **91**(1): 65-90.
31. Gibson SA, Thompson RN, Dickin AP. Ferropicrites: geochemical evidence for Fe-rich streaks in upwelling mantle plumes. *Earth and Planetary Science Letters* 2000, **174**(3): 355-374.
32. Milidragovic D, Francis D. Ca. 2.7Ga ferropicritic magmatism: A record of Fe-rich heterogeneities during Neoarchean global mantle melting. *Geochimica et Cosmochimica Acta* 2016, **185**: 44-63.
33. Zhang J, Liu Y, Ling W, Gao S. Pressure-dependent compatibility of iron in garnet: Insights into the origin of ferropicritic melt. *Geochimica et Cosmochimica Acta* 2017, **197**: 356-377.
34. Hanski EJ, Smolkin VF. Iron- and LREE-enriched mantle source for early Proterozoic intraplate magmatism as exemplified by the Pechenga ferropicrites, Kola Peninsula, Russia. *Lithos* 1995, **34**(1): 107-125.
35. Stone WE, Crocket JH, Dickin AP, Fleet ME. Origin of Archean ferropicrites: geochemical constraints from the Boston Creek Flow, Abitibi greenstone belt, Ontario, Canada. *Chemical Geology* 1995, **121**(1): 51-71.

- 446 36. Francis D, Ludden J, Johnstone R, Davis W. Picrite evidence for more Fe in  
447 Archean mantle reservoirs. *Earth and Planetary Science Letters* 1999, **167**(3):  
448 197-213.
- 449 37. Goldstein SB, Francis D. The Petrogenesis and Mantle Source of Archean  
450 Ferropicrites from the Western Superior Province, Ontario, Canada *Journal of*  
451 *Petrology* 2008, **49**(10): 1729-1753.
- 452 38. Valley JW. Oxygen isotopes in zircon. *Reviews in Mineralogy and Geochemistry*  
453 2003, **53**(1): 343-385.
- 454 39. Winchester JA, Floyd PA. Geochemical discrimination of different magma series  
455 and their differentiation products using immobile elements. *Chemical Geology*  
456 1977, **20**: 325-343.
- 457 40. Sun SS, McDonough WF. Chemical and isotopic systematics of oceanic basalts:  
458 implications for mantle composition and processes. *Geological Society, London,*  
459 *Special Publications* 1989, **42**(1): 313-345.
- 460 41. Arndt N. Komatiites, kimberlites, and boninites. *Journal of Geophysical Research:*  
461 *Solid Earth* 2003, **108**(B6): 2002JB002157.
- 462 42. Katz RF, Spiegelman M, Langmuir CH. A new parameterization of hydrous  
463 mantle melting. *Geochemistry, Geophysics, Geosystems* 2003, **4**(9):  
464 2002GC000433.

## 465 Acknowledgements

466 We thank S. Gibson for constructive discussions. This study was supported by the

467 National Natural Science Foundation of China (grant No. 41430207, 41372060,  
468 41572040) and the Fundamental Research Funds for the Central Universities of China  
469 (grant No. 2652018115). C.W. acknowledges Chinese Scholarship Council for the  
470 financial support during his visit to Durham University (grant No. 201606010063).

## 471 **Author contributions**

472 C.W. and S.S designed the project and wrote the manuscript. C.W., S.S., C.J.W. and  
473 J.D. conducted fieldwork. C.W., L.S. and X.-H.L performed all the analyses. All  
474 authors contributed to the interpretation of the results and the revision of the  
475 manuscript.

## 476 **Competing interests**

477 The authors declare no competing interests.

## 478 **Additional information**

479 **Supplementary information** is available in the online version of the paper.

480 **Correspondence and requests for materials** should be addressed to C.W. and S.S.

## 481 **Methods**

482 **In situ zircon U-Pb dating.** Zircon grains were extracted from crushed samples by  
483 standard heavy-liquid and magnetic techniques, and purified by hand-picking under a  
484 binocular microscope. The selected grains were mounted in epoxy resin and polished



485 down to about half-sections to expose the grain interiors, and then imaged under  
486 reflected and transmitted lights and by using CL. The CL images were acquired using  
487 a Panchromatic CL detector installed on a MIRA3 scanning electron microscope at  
488 MOE Key Laboratory of Orogenic Belts and Crustal Evolution, School of Earth and  
489 Space Sciences, Peking University, Beijing. Mineral inclusions in zircons were  
490 identified using an Oxford INCA-Synergy energy dispersive spectroscopy installed on  
491 a FEI FEG 650 scanning electron microscope (SEM-EDS) at Peking University.

492 Measurements of zircon U, Th and Pb isotopes were conducted using the  
493 CAMECA IMS-1280 secondary ion mass spectrometry (SIMS) at the Institute of  
494 Geology and Geophysics, Chinese Academy of Sciences (IGGCAS) in Beijing,  
495 following the standard procedures described in ref. 43. The primary  $O^{2-}$  ion beam spot  
496 is about  $20 \times 30 \mu m$  in size. Analyses of the standard zircon Plešovice were  
497 interspersed with unknown grains. Pb/U calibration was performed relative to zircon  
498 standard Plešovice<sup>44</sup>; U and Th concentrations were calibrated against zircon standard  
499 91500<sup>45</sup>. In order to monitor the external uncertainties of SIMS U-Pb zircon dating  
500 calibrated against Plešovice standard, an in-house zircon standard Qinghu was  
501 alternately analyzed as an unknown together with other unknown zircons. Fifteen  
502 measurements on Qinghu zircon yield a concordia age of  $159.9 \pm 1.2$  Ma, which is  
503 identical within error with the recommended value of  $159.5 \pm 0.2$  Ma<sup>46</sup>. A long-term  
504 uncertainty of 1.5% (1 relative standard deviation) for  $^{206}Pb/^{238}U$  measurements of the  
505 standard zircons was propagated to the unknowns. Measured compositions were  
506 corrected for common Pb using non-radiogenic  $^{204}Pb$ . Corrections are sufficiently

507 small to be insensitive to the choice of common Pb composition, and an average of  
508 present-day crustal composition<sup>47</sup> is used for the common Pb assuming that the  
509 common Pb is largely surface contamination introduced during sample preparation.  
510 Data reduction was carried out using the Isoplot/Ex ver. 3.0<sup>48</sup>. Uncertainties of  
511 individual analyses in data tables are reported at 1 $\sigma$  level.

512 **In situ zircon oxygen isotope analyses.** After U-Pb dating, the sample mount was  
513 re-ground and re-polished to ensure that any oxygen implanted in the zircon surface  
514 from the O<sup>2-</sup> beam used for U-Pb dating was removed. Zircon oxygen isotopes were  
515 measured using the CAMECA IMS-1280 SIMS at IGGCAS, following standard  
516 procedures described in ref. 49. The primary Cs<sup>+</sup> ion beam spot was 10  $\mu$ m in size.  
517 Oxygen isotopes were measured using multi-collection mode on two off-axis Faraday  
518 cups. The instrumental mass fractionation factor (IMF) was corrected using the zircon  
519 standard 91500 with a  $\delta^{18}\text{O}$  value of 9.9‰<sup>50</sup>. Measured  $^{18}\text{O}/^{16}\text{O}$  ratios were  
520 normalized using the Vienna Standard Mean Ocean Water compositions (VSMOW:  
521  $^{18}\text{O}/^{16}\text{O} = 0.0020052$ ), and then reported in standard per mil notation. A second zircon  
522 standard Qinghu was also analyzed as an unknown to ascertain the veracity of the  
523 IMF. Uncertainties on individual analyses are reported at 1 $\sigma$  level. The internal  
524 precision of a single analysis is generally better than 0.2‰ (2 $\sigma$ ) for  $^{18}\text{O}/^{16}\text{O}$  ratio. The  
525 external reproducibility of  $^{18}\text{O}/^{16}\text{O}$  ratios by repeated measurements of standard zircon  
526 is better than 0.40‰. Twenty-four measurements of Qinghu zircon standard during  
527 the course of this study yielded a weighted mean of  $\delta^{18}\text{O} = 5.38 \pm 0.12\text{‰}$  (2 $\sigma$ , n = 24),  
528 which is consistent within errors with the reported value of  $5.4 \pm 0.2\text{‰}$ <sup>46</sup>.

529 **In situ zircon Hf isotope analyses.** In situ zircon Hf isotope analyses of the dated  
530 sample were carried out using a Neptune multi-collector inductively coupled plasma  
531 mass spectrometry attached with a New Wave UP-213 laser-ablation system  
532 (LA-MC-ICPMS) at MLR Key Laboratory of Metallogeny and Mineral Assessment,  
533 Institute of Mineral Resources, Chinese Academy of Geological Sciences, Beijing.  
534 Analytical details are given in ref. 51. Laser spot size of 40  $\mu\text{m}$  was adopted for  
535 analyses and Helium gas was used as carrier gas to transport the laser ablated sample  
536 from the laser-ablation cell to the ICPMS torch via a mixing chamber mixed with  
537 Argon gas. Correction for the isobaric interferences of  $^{176}\text{Lu}$  and  $^{176}\text{Yb}$  on  $^{176}\text{Hf}$  was  
538 after ref. 51. Before the analyses, standard zircons (TEMORA, GJ1 and FM02) were  
539 analyzed and the efficacy of the correction method of isobaric interferences in ref. 51  
540 was tested to be efficient. Zircon GJ1 was used as the reference standard to monitor  
541 data quality during analyses, giving a weighted mean  $^{176}\text{Hf}/^{177}\text{Hf}$  ratio of  $0.282015 \pm$   
542  $9$  ( $2\sigma$ ,  $n = 9$ ), which is in accordance with the weighted mean  $^{176}\text{Hf}/^{177}\text{Hf}$  ratio of  
543  $0.282000 \pm 5$  ( $2\sigma$ ) measured by the solution analysis method<sup>52</sup>.

544 **In situ zircon trace element analyses.** Measurement of trace elements in zircons  
545 were carried out on an Agilent-7500a quadrupole inductively coupled plasma mass  
546 spectrometer coupled with a New Wave UP-193 solid-state laser-ablation system  
547 (LA-ICPMS) in the Geological Lab Center, China University of Geosciences, Beijing  
548 (CUGB). A laser spot size of 36  $\mu\text{m}$ , laser energy density of  $8.5 \text{ J cm}^{-2}$  and a  
549 repetition rate of 10 Hz were used for analyses. The ablated sample material was  
550 carried into the ICPMS system by high-purity helium gas. Calibrations for element

551 concentration were carried out using NIST 610 glass and Harvard standard zircon  
552 91500 as external standards, with recommended values taken from refs. 45 and 53 and  
553 using  $^{29}\text{Si}$  as an internal standard. NIST 612 and 614 glasses served as monitoring  
554 standards at the same time. The analytical accuracy for trace elements in zircon is  
555 better than  $\pm 10\%$  with abundances  $> 10$  ppm, and  $\pm 15\%$  with abundances  $< 10$  ppm.

556 **Bulk-rock major and trace element analyses.** All the samples are fresh cuttings  
557 away from late veinlets, with any surface contaminants trimmed off before being  
558 thoroughly cleaned. Fresh portions of the trimmed samples were crushed into 1–2 cm  
559 size chips using a percussion mill. These rock fragments were ultrasonically cleaned  
560 in Milli-Q water, dried and powdered in a thoroughly cleaned agate mill to 200 mesh  
561 in the clean laboratory at the Langfang Regional Geological Survey, China. Bulk-rock  
562 major and trace element analyses were done in the Geological Lab Center, CUGB  
563 following the procedures described in ref. 54. Major elements were analyzed on a  
564 Leeman Prodigy inductively coupled plasma-optical emission spectroscopy (ICP-OES)  
565 system with high dispersion Echelle optics. Based on rock standards AGV-2, W-2 (US  
566 Geological Survey: USGS), GSR-1 and GSR-3 (national geological standard  
567 reference material of China), the analytical precisions ( $1\sigma$ ) for most major element  
568 oxides are better than 1% with the exception of  $\text{TiO}_2$  ( $\sim 1.5\%$ ) and  $\text{P}_2\text{O}_5$  ( $\sim 2.0\%$ ). Loss  
569 on ignition (LOI) was determined by placing 1 g of samples in the furnace at  $1000^\circ\text{C}$   
570 for a few hours and then reweighting the cooled samples.

571 Bulk-rock trace elements were analyzed using an Agilent-7500a quadrupole  
572 inductively coupled plasma mass spectrometry (ICPMS). About 35 mg powder of

each sample was dissolved in distilled acid mixture (1:1 HF + HNO<sub>3</sub>) with Teflon digesting vessels and heated on a hot-plate at 195 °C for 48 hours using high-pressure bombs for digestion/dissolution. The sample was then evaporated to incipient dryness, refluxed with 1 mL of 6 N HNO<sub>3</sub> and heated again to incipient dryness. The sample was again dissolved in 2 mL of 3 N HNO<sub>3</sub> and heated at 165 °C for further 24 hours to guarantee complete digestion/dissolution. The sample was finally diluted with Milli-Q water to a dilution factor of 2,000 in 2% HNO<sub>3</sub> solution for ICPMS analyses. Rock standards AGV-2, W-2 and BHVO-2 (USGS) were used to monitor the analytical accuracy and precision. Analytical accuracy, as indicated by relative difference between measured and recommended values is better than 5% for most elements, and 10 ~ 15% for Cu, Zn, Gd, and Ta.

**Calculation of Mg# and liquidus temperatures for melts in equilibrium with meta-cumulates.** Cumulus minerals should be in equilibrium with the melts from which they precipitated and the liquidus temperature of basaltic melts is proportional to the MgO contents in the melts<sup>55-57</sup>. Thus the Mg# and liquidus temperatures of the melts crystallizing cumulus minerals can be calculated using the well-established Fe-Mg exchange coefficients ( $K_D(\text{Fe-Mg})^{\text{mineral-liquid}} = (\text{Mg}^{\text{liquid}}/\text{Fe}^{2+\text{liquid}})/(\text{Mg}^{\text{mineral}}/\text{Fe}^{2+\text{mineral}})$ ). Since meta-cumulates experienced HP granulite-facies metamorphism at the end of the Archaean and Fe-Mg re-exchanges should have occurred between minerals during this high-grade metamorphism, the compositions of pyroxenes or olivines present in the meta-cumulates cannot represent primitive compositions in equilibrium with the melts. However, the

595  $K_D(\text{Fe-Mg})^{\text{Cpx-liquid}}$  ( $0.28 \pm 0.08$ ) is similar to the  $K_D(\text{Fe-Mg})^{\text{Opx-liquid}}$  ( $0.29 \pm 0.06$ ) and  
 596 the  $K_D(\text{Fe-Mg})^{\text{Ol-liquid}}$  ( $0.30 \pm 0.03$ )<sup>58,59</sup>, which allows us to use the bulk-rock Mg# of  
 597 the meta-cumulates to estimate the nature of their parental magma. Because of the  
 598 effect of trapped liquid crystallization on cumulus mineral compositions<sup>60</sup>, the  
 599 calculated Mg# and liquidus temperatures should represent minimum estimates for the  
 600 equilibrated melts. The calculations are as following:  
 601  $Mg\#(\text{equilibrated melts}) = 1/[1/Mg\#(\text{bulk-rock}) - 1/Kd(\text{Fe-Mg}) + 1]$ , where  
 602  $Kd(\text{Fe-Mg}) = 0.28$  for meta-websterites;  $0.30$  for meta-lherzolites;  
 603  $T_{\text{liquidus}} (^{\circ}\text{C}) = 1,066 + 12.067Mg\# + 312.3 (Mg\#)^2$ ;  
 604  $Mg\# = \text{molar } 100 * Mg / (Mg + Fe)$ .

## 605 Data availability

606 The authors declare that all data supporting the findings of this study are available  
 607 within the main text, figures and Supplementary Information files.

## 608 References

- 609 43. Li X-H, Liu Y, Li Q-L, Guo C-H, Chamberlain KR. Precise determination of  
 610 Phanerozoic zircon Pb/Pb age by multicollector SIMS without external  
 611 standardization. *Geochemistry, Geophysics, Geosystems* 2009, **10**(4): Q04010.  
 612 44. Sláma J, Košler J, Condon DJ, Crowley JL, Gerdes A, Hanchar JM, *et al.*  
 613 Plešovice zircon—a new natural reference material for U–Pb and Hf isotopic  
 614 microanalysis. *Chemical Geology* 2008, **249**(1-2): 1-35.

- 615 45. Wiedenbeck M, Allé P, Corfu F, Griffin WL, Meier M, Oberli F, *et al.* Three  
616 natural zircon standards for U-Th-Pb, Lu-Hf, trace element and REE analyses.  
617 *Geostandards Newsletter* 1995, **19**(1): 1-23.
- 618 46. Li X-H, Tang G, Gong B, Yang Y, Hou K, Hu Z, *et al.* Qinghu zircon: A working  
619 reference for microbeam analysis of U-Pb age and Hf and O isotopes. *Chinese*  
620 *Science Bulletin* 2013, **58**(36): 4647-4654.
- 621 47. Stacey Jt, Kramers J. Approximation of terrestrial lead isotope evolution by a  
622 two-stage model. *Earth and Planetary Science Letters* 1975, **26**(2): 207-221.
- 623 48. Ludwig KR. *User's manual for Isoplot 3.0: A geochronological toolkit for*  
624 *Microsoft Excel*. Berkeley Geochronology Centre, Special Publication, 2003.
- 625 49. Li X-H, Li W-X, Li Q-L, Wang X-C, Liu Y, Yang Y-H. Petrogenesis and tectonic  
626 significance of the ~850 Ma Gangbian alkaline complex in South China:  
627 Evidence from in situ zircon U-Pb dating, Hf-O isotopes and whole-rock  
628 geochemistry. *Lithos* 2010, **114**(1-2): 1-15.
- 629 50. Wiedenbeck M, Hanchar JM, Peck WH, Sylvester P, Valley J, Whitehouse M, *et al.*  
630 Further characterisation of the 91500 zircon crystal. *Geostandards and*  
631 *Geoanalytical Research* 2004, **28**(1): 9-39.
- 632 51. Wu F-Y, Yang Y-H, Xie L-W, Yang J-H, Xu P. Hf isotopic compositions of the  
633 standard zircons and baddeleyites used in U-Pb geochronology. *Chemical*  
634 *Geology* 2006, **234**(1-2): 105-126.
- 635 52. Morel MLA, Nebel O, Nebel-Jacobsen YJ, Miller JS, Vroon PZ. Hafnium isotope  
636 characterization of the GJ-1 zircon reference material by solution and

- 637 laser-ablation MC-ICPMS. *Chemical Geology* 2008, **255**(1–2): 231-235.
- 638 53. Pearce NJG, Perkins WT, Westgate JA, Gorton MP, Jackson SE, Neal CR, *et al.* A  
639 Compilation of New and Published Major and Trace Element Data for NIST SRM  
640 610 and NIST SRM 612 Glass Reference Materials. *Geostandards Newsletter*  
641 1997, **21**(1): 115-144.
- 642 54. Song SG, Su L, Li XH, Zhang GB, Niu YL, Zhang LF. Tracing the 850-Ma  
643 continental flood basalts from a piece of subducted continental crust in the North  
644 Qaidam UHPM belt, NW China. *Precambrian Research* 2010, **183**(4): 805-816.
- 645 55. Weaver SJ, Langmuir CH. Calculation of phase equilibrium in mineral-melt  
646 systems. *Computers & Geosciences* 1990, **16**(1): 1-19.
- 647 56. Niu Y. Mantle melting and melt extraction processes beneath ocean ridges:  
648 Evidence from abyssal peridotites. *Journal of Petrology* 1997, **38**(8): 1047-1074.
- 649 57. Niu Y, Gilmore T, Mackie S, Greig A, Bach W. Mineral chemistry, whole-rock  
650 compositions, and petrogenesis of Leg 176 gabbros: data and discussion.  
651 Proceedings of the Ocean Drilling Program, Scientific Results; 2002: Ocean  
652 Drilling Program College Station, TX; 2002. p. 1-60.
- 653 58. Roeder PL, Emslie RF. Olivine-liquid equilibrium. *Contributions to Mineralogy*  
654 *and Petrology* 1970, **29**(4): 275-289.
- 655 59. Putirka KD. Thermometers and barometers for volcanic systems. *Reviews in*  
656 *Mineralogy and Geochemistry* 2008, **69**(1): 61-120.
- 657 60. Barnes SJ. The effect of trapped liquid crystallization on cumulus mineral  
658 compositions in layered intrusions. *Contributions to Mineralogy and Petrology*



659 1986, **93**(4): 524-531.

Figure 1

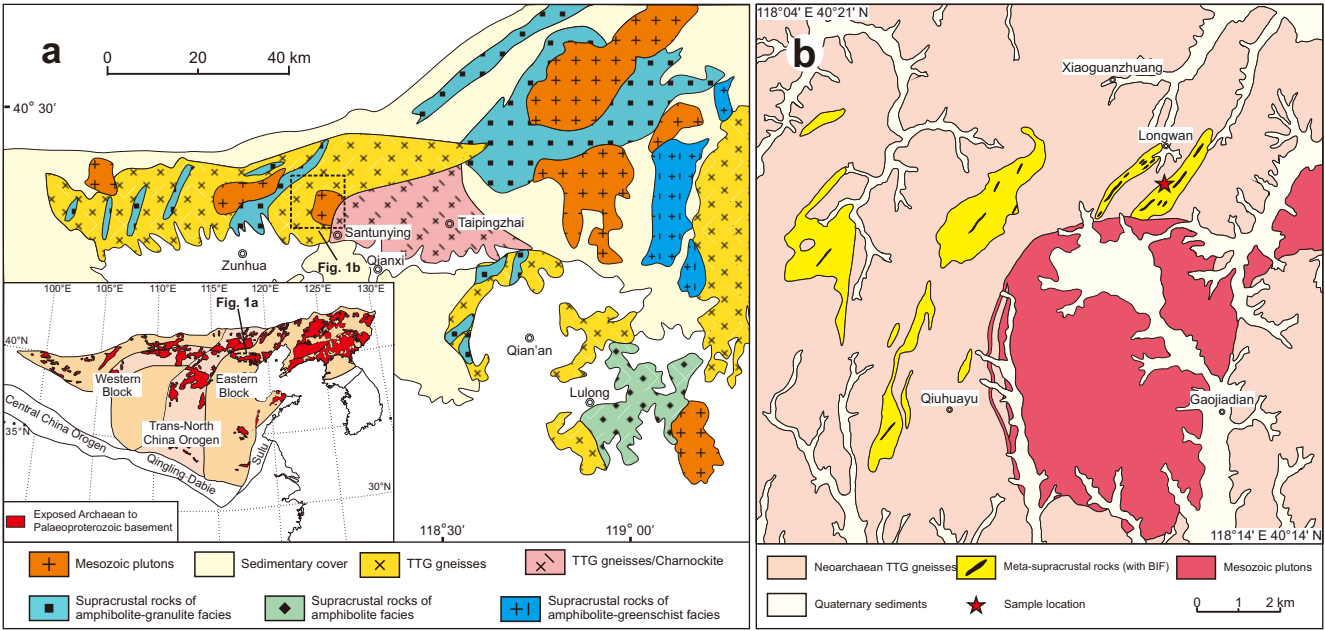


# Figure 2

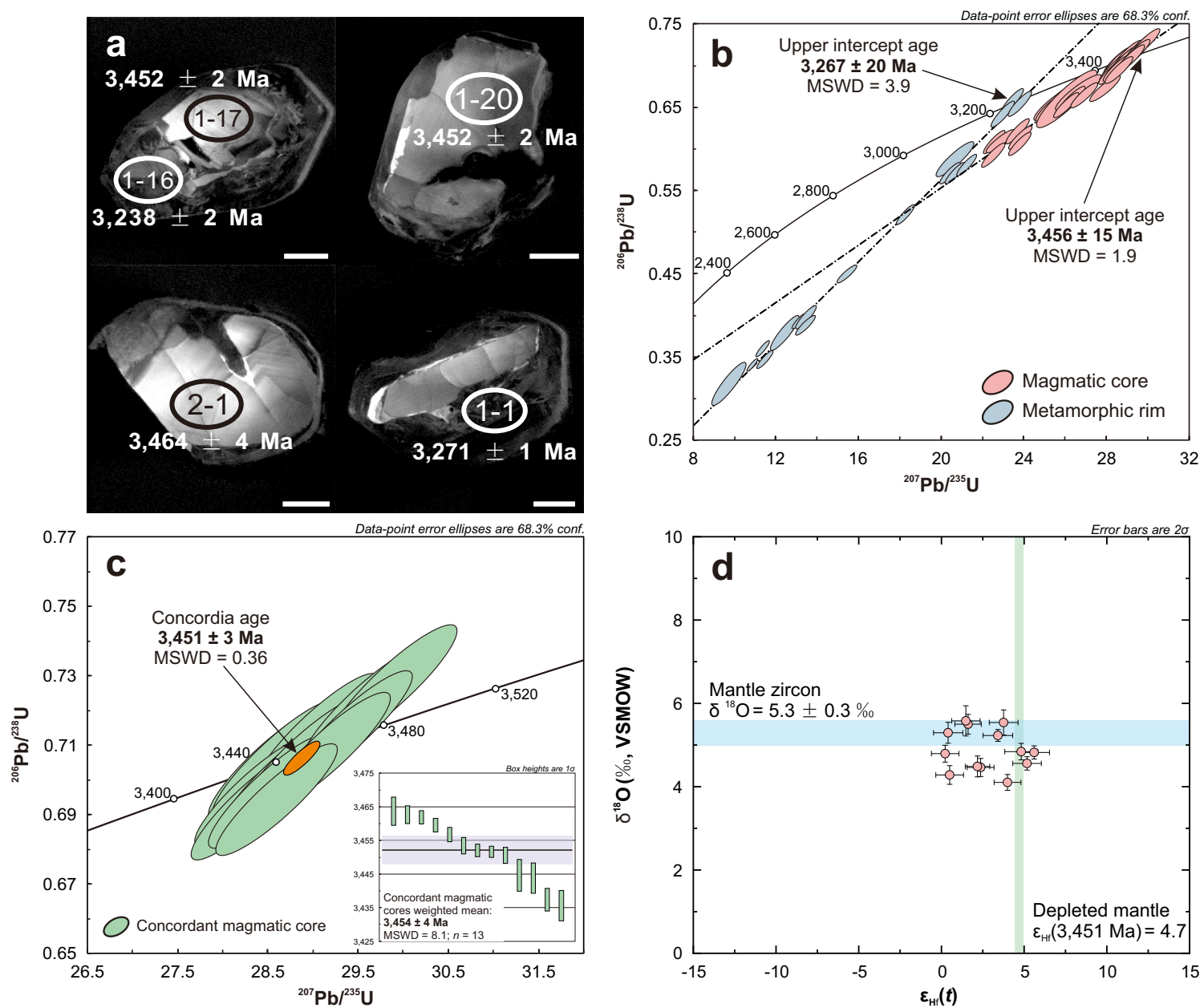


# Figure 3

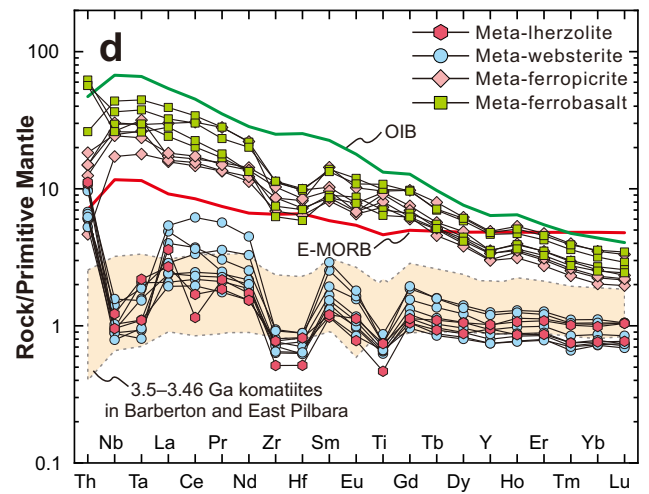
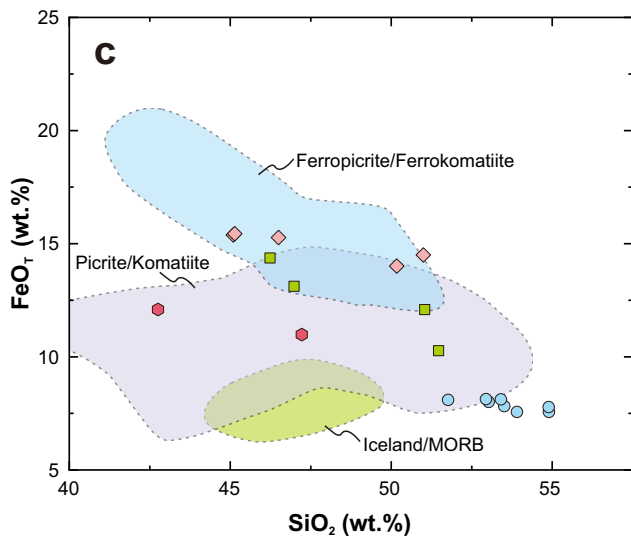
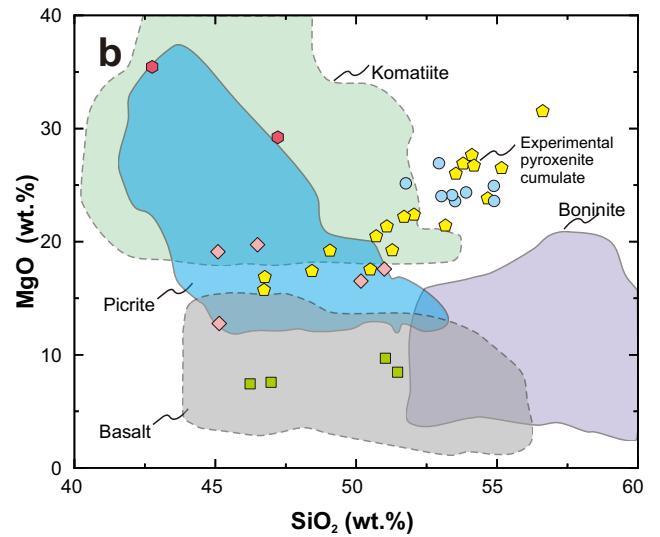
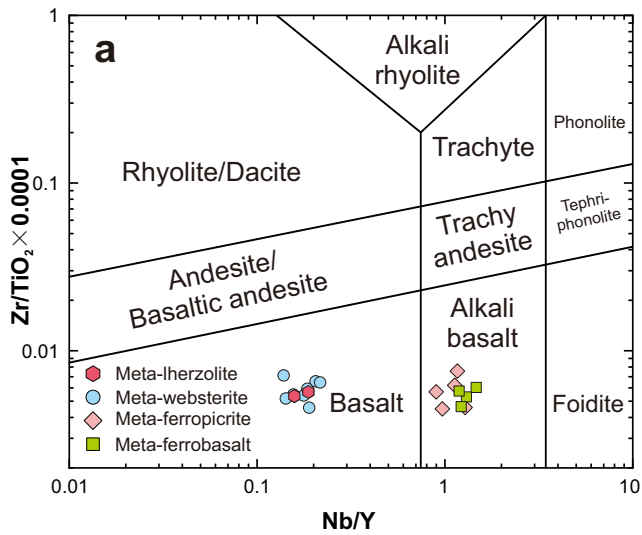


Figure 4

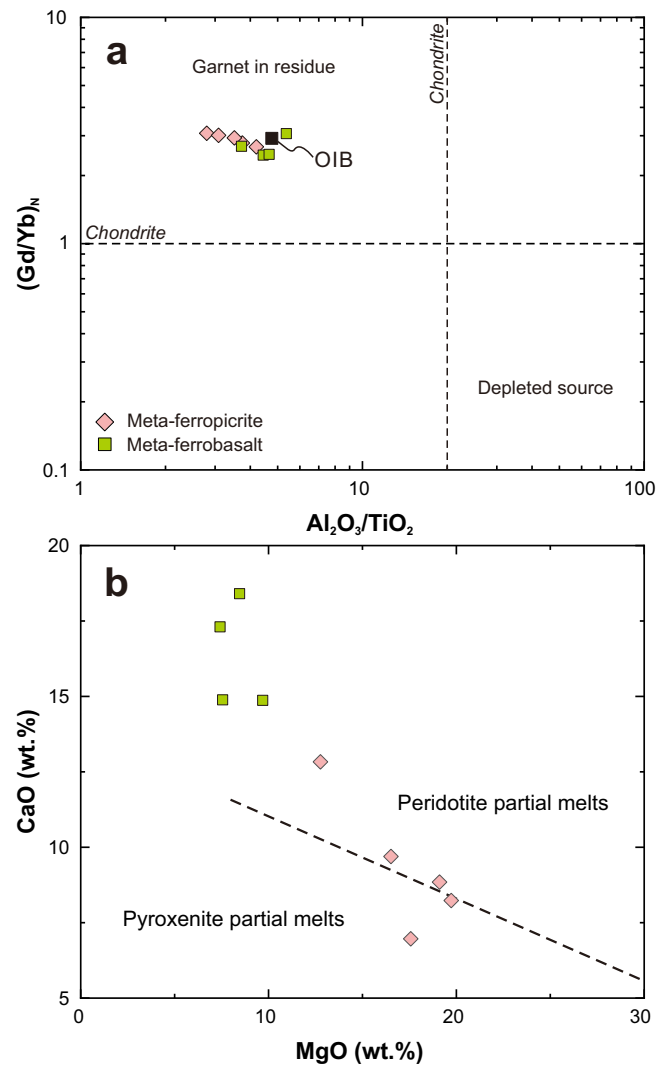


Figure 5

